Journal Name

Dynamic Article Links ►

Cite this: DOI: 10.1039/c0xx00000x

www.rsc.org/xxxxxx

ARTICLE TYPE

Water Flow Enhancement in Hydrophilic Nanochannels

Kah Peng Lee, Hannah Leese and Davide Mattia*

Received (in XXX, XXX) Xth XXXXXXXXX 20XX, Accepted Xth XXXXXXXXX 20XX
DOI: 10.1039/b000000x

All published reports on fluid flow enhancement and water slippage are associated with hydrophobic surfaces, such as carbon nanotubes. Here, we investigate water flow in hydrophilic alumina nanochannels with diameters ranging from 20 nm to 100 nm. For the smallest channels tested, the water permeability is more than double than the theoretical prediction using the Hagen-Poiseuille equation. Though such an enhancement is significantly smaller than what has been measured in carbon nanotubes, it clearly shows that flow enhancement and water slippage occurs on hydrophilic surfaces as well, contrary to existing theoretical models. To the authors' knowledge, it is the first experimental demonstration of water slippage on hydrophilic surfaces. The results show the dependence of the flow enhancement on the surface chemistry, channel diameter and length.

Introduction

Liquid flow through nanoporous media has been studied in disciplines as diverse as membrane science, soil permeability and cell physiology. In all these fields, though, the emphasis has been on the macroscopic outcome, often neglecting the effects of intermolecular forces and liquid-pore wall physicochemical interactions on liquid behaviour. The availability of carbon nanotubes (CNTs) as a platform for mass transport studies at the nanoscale has generated a large number of experimental and molecular dynamics (MD) studies, which have shown unexpected fluid behaviours compared to the macroscale.[1] The most striking one has been the observation of several orders of magnitude higher liquid flow velocities compared to the no-slip Hagen-Poiseuille (HP) equation,[2] defined as:

$$Q_{HP} = \frac{\pi D^4 \Delta P}{128 \mu L} \quad (1)$$

where Q_{HP} is the theoretical volumetric flow rate, D is the tube diameter, μ is the absolute viscosity, ΔP is the pressure drop, and L is the length of the tube. In all studies published so far, the flow enhancement factor, ε, has been used as a measure of the deviation of experimental results from the Hagen-Poiseuille equation:

$$\varepsilon = \frac{Q_{exp}}{Q_{HP}} \quad (2)$$

where Q_{exp} is the numerically or experimentally observed volumetric flow rate.

The modelling and experimental results vary significantly, with flow enhancements as small as 10,[3] and as large as ~10^5.[4, 5] The large variation in results can be attributed to significant differences in tube diameter, length, surface chemistry and structure of the different nanotubes tested.[6-8] In general, flow enhancement increases with decreasing tube diameter,[9, 10] down to the transition from the continuum to the sub-continuum regime (between 0.8 nm to 2.0 nm).[11, 12] Flow measurements in larger carbon nanotubes (> 100 nm in diameter) showed no measurable enhancement.[13] In the sub-continuum range, where Equation 1 no longer applies, Equation 2 has been used nonetheless as an indication of the flow behaviour. Ballistic-type transport, [14-17] and the dependence of flow enhancement on the tube's length, above a certain length threshold, have been some of the most notable results.[18] The latter result, obtained via MD simulations, has been indirectly confirmed by very high flow enhancement values, in the 10^4-10^5 range, obtained experimentally for very long CNTs.[4, 10, 19] The impact of different tube surface chemistry and structure on flow enhancement has been somewhat less investigated, due to both computational and experimental limitations. Nonetheless, some interesting results have been published. A flow enhancement of about 35 has been observed for water flowing through 44 nm diameter nanopipes, or nanotubes with a turbostratic (disordered) graphitic structure.[20] While in this experiment it was not possible to separate the effect on enhancement of tube diameter from wall structure, capillary filling and condensation experiments on similar tubes suggest that by changing the surface chemistry and structure of the CNTs it is possible to control whether the liquid will enter the tube or not.[21, 22] MD simulations on tubes with the structure of a CNT but surface potentials of hydrophilic Si support this result, with a significant reduction in the flow velocity and enhancement.[23] These results point to the fact that the high flow enhancements observed are a combination of tube size and wall surface chemistry, although an explicit relation between the former and the latter has not yet been presented.[1, 2, 6, 7] It is generally accepted that the origin of the high flow rates observed resides in the unfavourable interaction of water with the hydrophobic surface of

the carbon nanotubes.[23, 24] This would result in the slippage of water molecules at the CNT wall, leading to high flow velocities.[25] Water slip on hydrophobic surfaces is a well-documented phenomenon,[26] whereas its occurrence on hydrophilic surfaces is still a matter of debate.[27] Recent MD simulations, though, point to the fact that water can slip on hydrophilic surfaces, due to spontaneous liquid molecule migration from one adsorption site to the adjacent one.[28] Experimental flow measurements in hydrophilic nanochannels have, so far, focused on the effect of surface changes on the flow in silica nanotubes or nanochannels, with no specific velocity or flow enhancement values reported.[29-33] MD studies comparing the surface diffusion of water molecules through nano-sized slits of hydrophobic graphene and hydrophilic titanium oxide have found that the diffusion coefficients are of the same order of magnitude, with the former about twice the latter.[34, 35]

Anodized alumina membranes (AAMs) have a highly self-ordered pore structure consisting of straight nanochannels with narrow pore size distribution and pore diameter varying linearly with the anodization voltage.[36] By controlling the other process parameters it is also possible to control the porosity and the membrane thickness.[37] In this paper, a systematic study of pressure-driven water flow through hydrophilic AAMs with pore diameters ranging from 100 nm to 20 nm is reported. Results show that significant water flow enhancement values can be obtained also in hydrophilic nanochannels, with increasing values for decreasing channel size.

Methodology

AAMs fabrication procedures

AAMs were prepared based on a well-established 2–step potentiostatic anodization method.[38] Firstly, an aluminium sheet (99.99%, 0.25 mm thickness, Alfa Aesar) was cut into circular pieces of 10 mm diameter and annealed in air at 500 °C (CWF1100, Carbolite) for an hour. Then, they were cleaned by ultra-sonication in acetone (HPLC grade, 99.5+%, Fisher) for 10 minutes. The cleaned aluminium sheets were electropolished in a solution of perchloric acid (60-62%, Fisher) and ethanol (96%, Fisher) in the volumetric ratio of 1 : 4. Using a dry ice-acetone bath to maintain the temperature (< – 50 °C), the electropolishing was performed at 20 V for 15 minutes to obtain a mirror-like shiny surface.

Then, the aluminium substrates were anodized in 0.3M oxalic acid, using stainless steel (SS316 grade) as the cathode. The potentiostatic anodization voltage ranged from 25 V to 80 V, whereas the temperature was regulated from 13 °C to 0 °C, depending on the anodization voltage. The alumina formed from the one-hour first-step anodization was then removed by wet chemical etching using a 1 : 1 mixture of 6 wt% phosphoric acid and 1.8 wt% chromic acid at 60 °C for 20 minutes. Having formed the porous template, the second-step anodization was performed immediately under the same conditions as the first step, but for a longer period of 10 to 12 hours.

The residual non-anodized aluminium substrate was removed by a reaction with copper(II) chloride in a 1 : 1 solution of 0.2 M copper(II) chloride to 20% hydrochloric acid. The oxide barrier layer was etched away by 6 wt% phosphoric acid in an electrochemical setup to control the etching process, *i.e.* ensuring the pores were completely opened through but not widened (over etched). [39] In the setup, the barrier layer side of the AAMs was in contact with phosphoric acid, whereas the porous side was in contact with 0.2 M potassium chloride solution. By placing an electrode in each solution, a current could be detected when the pores started to open during the etching. Adequate etching was achieved when the current reached plateau.

AAM pore structure characterization

Two AAMs were prepared for each anodization voltage. The resulting free standing AAMs were characterized using a Hitachi S-4300 field emission scanning electron microscope (FESEM). Statistical image analysis of SEM micrographs using ImageJ software yielded the pore structural characteristics, i.e. pore diameter, pore circularity, porosity and pore size distribution. Using ImageJ, the micrographs obtained were processed first by thresholding, i.e. converting the greyscale image into a binary (black and white) image (Figure 1e). The software then identifies each pore and quantifies the area, perimeter, feret's diameter and circularity of each pore (Figure 1f). Table 1 shows the information obtained from ImageJ based on the pores within the circled area in Figure 1f. Due to the feret's diameter being the longest distance between any two tangents contacting the pore boundary, it overestimated the effective pore diameter. Thus, the feret's diameter was compensated by circularity to obtain the effective pore diameter, which gives values in good agreement with previous reported literature (as discussed later). To calculate pore diameter, the pores at the edges of the bracketed area were excluded, whereas for porosity estimation, they were included.

Table 1 Example of information obtained from image analysis based on Figure 1f

Pore label	Area (nm^2)	Perimeter (nm)	Feret's diameter (nm)	Circularity (-)	Effective pore diameter (nm)
A	1683	149	50	0.95	47
B	1887	159	52	0.94	49
C	1775	154	50	0.94	47
D	1630	149	48	0.93	45
E	1749	152	50	0.95	47
F	1782	152	51	0.97	50
G	1795	154	50	0.95	47

Fluid Flow Measurement

To conduct the fluid flow measurements through the AAMs, each membrane was securely clamped in a custom-made membrane holder, consisting of two stainless steel flanges with silicone rubber annuluses (5 mm inner diameter effective area for water permeation) to prevent membrane fracture and to ensure a tight sealing, preventing water slippage around the membrane. For measurements at higher pressures, the membrane was supported using a highly porous Vyon polypropylene mesh, with no appreciable effect on the flow. The membrane holder was then connected to the fluid flow measurement apparatus which was built using Swagelok® stainless steel quarter inch tubing parts (Figure 2a). Pressure transducers (Swagelok industrial standard, ±5kPa error) were placed before and after the membrane holder, recording the pressure loss across the membrane. Since viscosity is temperature-dependent, a thermocouple (Omega, Type T) was attached to the rig.

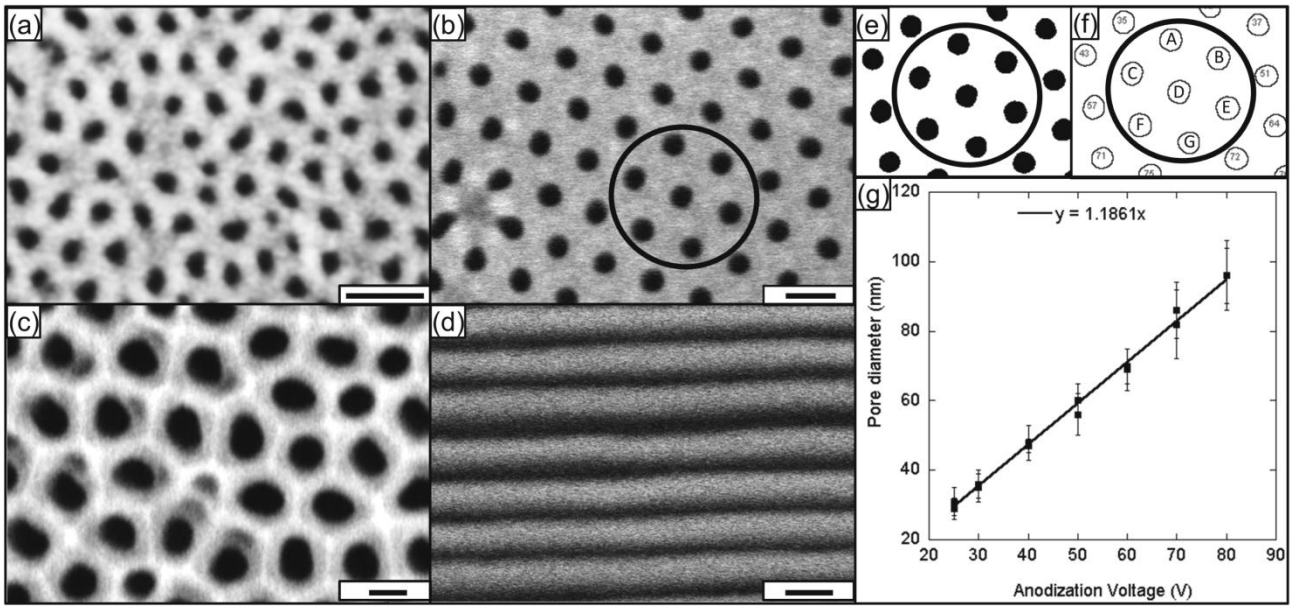

Fig. 1 SEM micrographs of anodized alumina membranes (AAM) anodized at (a) 25 V; (b) 40 V; and (c) 80 V; (d) cross-section of AAM fabricated at 50 V showing straight-through nanochannels. (e) Section of 2b after threshold processing and (f) after image statistical analysis on processed image where information for each pore in the circled region is presented in Table 1. All scale bars correspond to 100 nm. (g) Linear relationship between anodizing voltage and pore diameter during anodization process.

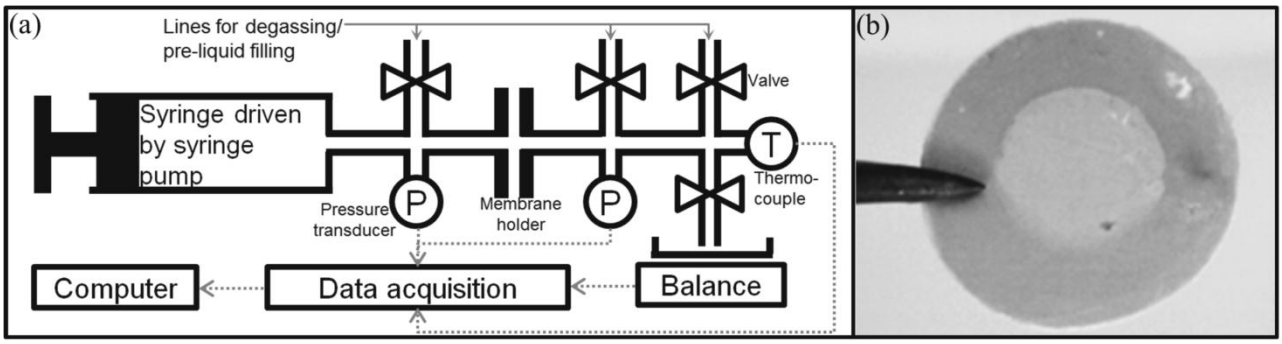

Fig. 2 (a) Schematic of fluid flow measurement setup; (b) Membrane with a 5 mm diameter circular water mark after flow measurement.

Several precautions were taken to ensure accurate measurements. Ultrapure water (Milli-Q, 18.2 MΩ cm^{-1} at 25 °C) in a stainless steel syringe with 225 ml capacity was driven by a high force syringe pump (Nexus 6000). Before starting a flow measurement, the system was pre-filled with water and air bubbles were purged away. To check the effectiveness of sealing, the AAMs were placed into the membrane holder prior to oxide barrier layer removal (the pores are blocked). Even at a pressure of 700 kPa, water flow was completely blocked. In addition, in a normal run, a visible 5mm diameter circular wetted region on the membrane was noticed, ensuring a good sealing around the effective permeation area (Figure 2b).

The key variable measured in the fluid flow experiments was the steady-state pressure difference across the membrane, at an imposed water flow rate. For each membrane, four flow rate settings were tested and each run was for at least 45 minutes after the pressure had stabilized. The water permeate was collected in a beaker on a high precision balance (Mettler Toledo, MS304S/01, sensitivity up to 0.1mg). The beaker was pre-filled with some oil to minimise water loss by evaporation. All real-time measurements, i.e. pressure, temperature and mass of water permeate were recorded via a data acquisition system.

Results and discussion

AAM pore structure and wettability

Figure 1 shows SEM micrographs of several membranes, ranging from 25 V to 80 V. In agreement with previous findings,[37] a linear correlation between the pore diameter and the anodization voltage was observed with a gradient of 1.19 nm V^{-1} as shown in Figure 1g. The AAMs fabricated in oxalic acid electrolyte exhibit an optimum self-ordered structure at 40 V, with a narrow pore size distribution (Figure 1b). For lower and higher anodization voltages slightly wider pore size distributions were obtained, Figures 1a and 1c respectively. However, in each membrane, more than 90% of the pores size falls into a ±15% deviation span of the mean pore diameter (Figure 3).

The contact angle of water on the surface of AAMs was used to calculate the Young's contact angle for the anodized alumina, i.e. without the contribution of the air present in the pores.[40, 41] The obtained value, 12±2°, is in agreement with literature values for non-porous alumina. [42]

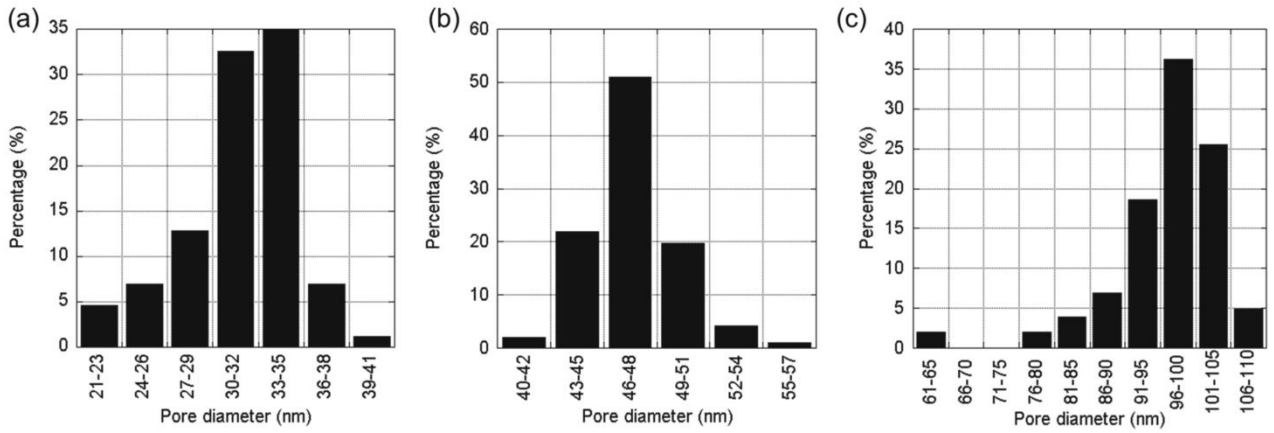

Fig. 3 Pore diameter distribution of AAMs fabricated at (a) 25 V; (b) 40 V and (c) 80 V.

AAM theoretical permeability

For a membrane consisting of straight channels, the HP equation can be rewritten as:

$$\frac{J_{HP}}{\Delta P} = \frac{\phi D_p^2}{32\tau} \quad (3)$$

where J_{HP} is the theoretical volumetric flux, ϕ is porosity, D_p is the average pore diameter and τ is tortuosity. The left side of equation (3) corresponds to the theoretical permeability of a membrane. The terms on the right hand side of the equation can all be measured experimentally: porosity and average pore diameter have been obtained from statistical image analysis of the AAM micrographs. The nanochannel length corresponds to the membrane thickness, which has been measured using a micrometre with 5 μm sensitivity. As shown in Figure 1d, the nanochannels in the AAMs are straight, yielding $\tau = 1$. In Table 2, the theoretical permeability for each membrane has been tabulated.

AAM experimental permeability

Figure 4a shows an example of data recorded from a fluid flow measurement of a 40 V membrane. The gradient of the mass profile at each stabilized pressure is the mass flow rate. As shown in Figure 4b, the mass flow rate obtained was then plotted against the corresponding stabilized pressure. Due to the varying room temperature of the laboratory, the flow rate was adjusted based on the recorded temperature and normalized to 25 ºC. A positive linear relationship was observed between water flow rate and pressure loss, with a high regression factor, consistently higher than 0.98. The slightly negative y-axis intercept obtained in Figure 4b accounts for the small pressure loss along the tubing and also the Vyon porous polypropylene mesh support. The gradient of the plot in Figure 4b was then normalized by the effective membrane area to obtain the experimental permeability, $J_{exp}/\Delta P$, which was then compared to the theoretical permeability. In Table 2, the experimental permeability of each membrane has been listed.

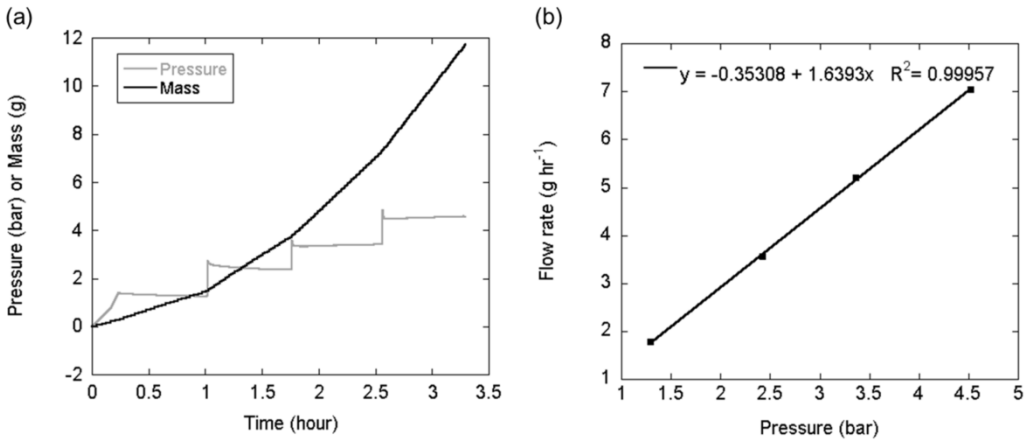

Fig. 4 Data recorded during a fluid flow measurement of a 40 V AAM: (a) Pressure difference and mass of water profiles showing four stabilized pressure regions and super-imposed flow rates; (b) plot of flow rate normalised with viscosity at 25 °C against the measured pressure.

Flow enhancement factor

The flow enhancement, as defined in Equation 2, is larger than one for all the AAM pore diameters examined and increases with decreasing pore diameter (Figure 5a). The error bars for the flow enhancement result from the error accumulation of all measuring devices, as discussed earlier in the text, while those for the pore diameters arise from statistical image analysis of SEM micrographs. In Figure 5b, the whole data set is presented (nearly 1300 data points), highlighting the fact that each membrane consists of a distribution, albeit narrow, of pore diameters. A summary of pore structure characteristics, theoretical and experimental permeabilities, as well as flow enhancement factors

for all tested membranes can be found in Table 2.

As shown in both plots in Figure 5, a significant flow enhancement was observed for the membranes with smaller pore diameters. As expected, the enhancement decreases with increasing pore diameter, with $\varepsilon \rightarrow 1$ for $D_p \rightarrow 100$ nm. This trend, where the flow enhancement factor is decreasing with increasing pore/tube diameter is in good agreement with both MD,[11, 12, 23] and experimental results. [13] It is apparent from these results that the flow enhancements observed for water through alumina nanochannels are much smaller than those reported for CNTs. Though small, the flow enhancements reported here are nonetheless larger than unity, signifying that even for hydrophilic materials high flow rates can be obtained for channels in the nanometre range.

Table 2 The ratio of experimental permeability to theoretical permeability yields the flow enhancement factor.

Membrane		ϕ	D_p[a]	L[b]	$J_{HP}/\Delta P$[c]	$J_{exp}/\Delta P$[d]	ε[e]
No.	Voltage	(-)	(nm)	(μm)	($\times 10^{-10}$ m^3 m^{-2} s^{-1} Pa^{-1})		(-)
1	25V	0.121	29±3	55±5	0.65±0.22	1.71±0.09	2.64±0.77
2	25V	0.142	31±4	55±5	0.87±0.35	2.24±0.12	2.57±0.95
3	30V	0.157	35±4	60±5	1.12±0.40	2.42±0.13	2.15±0.68
4	30V	0.153	36±4	65±5	1.07±0.36	2.21±0.12	2.07±0.30
5	40V	0.149	48±5	80±5	1.51±0.45	2.32±0.12	1.54±0.41
6	40V	0.153	47±2	80±5	1.48±0.24	2.32±0.12	1.57±0.28
7	50V	0.166	56±6	80±5	2.28±0.70	2.86±0.15	1.25±0.34
8	50V	0.167	60±5	105±5	2.01±0.47	2.47±0.13	1.23±0.28
9	60V	0.155	70±5	130±5	2.05±0.40	2.34±0.12	1.14±0.23
10	60V	0.155	69±6	135±5	1.92±0.44	2.18±0.11	1.14±0.25
11	70V	0.175	86±8	115±5	3.95±0.98	4.06±0.21	1.03±0.24
12	70V	0.166	82±10	130±5	3.01±0.93	3.26±0.17	1.08±0.29
13	80V	0.178	96±8	145±5	3.97±0.85	3.92±0.21	0.99±0.21
14	80V	0.168	96±10	120±5	4.53±1.23	4.67±0.25	1.03±0.26

[a] The presented error is the standard deviation.

[b] The error span for membrane thickness is based on micrometre sensitivity.

[c] The theoretical permeability was calculated using equation (3). The viscosity of water at 25 °C, 0.891 mPa.s was used. The error span is based on the errors in pore diameter and membrane thickness.

[d] The experimental permeability was normalized to viscosity at 25 °C. The error span for experimental permeability is based on the sensitivity of the pressure transducers.

[e] The error span for flow enhancement factor is the results of errors propagation of the variables above.

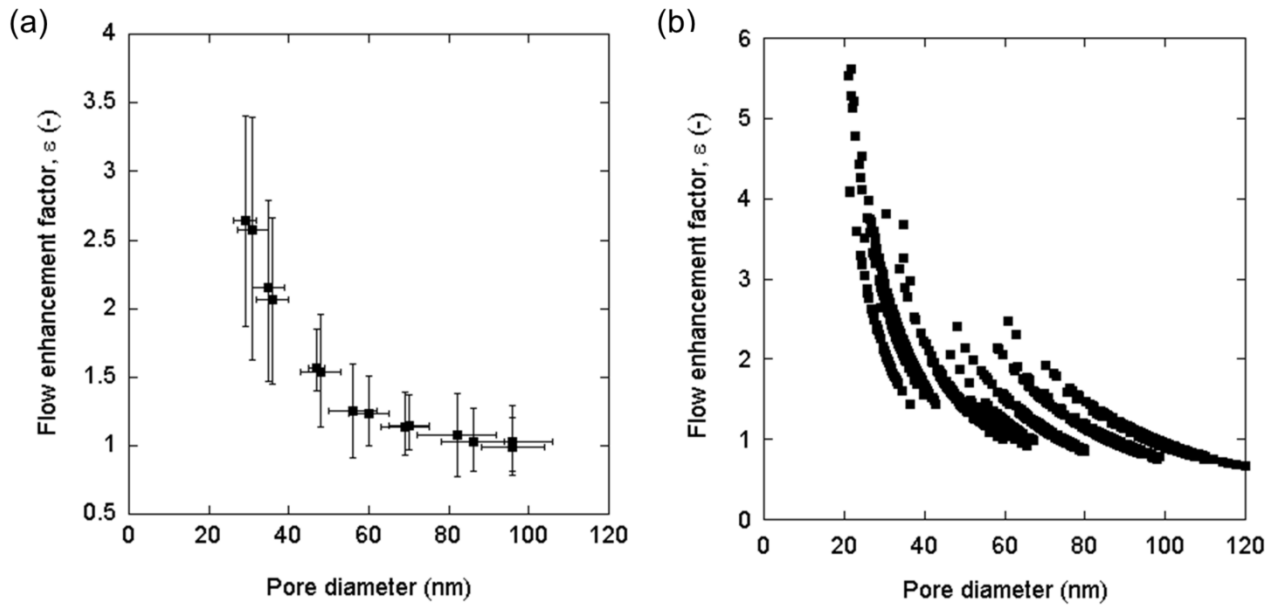

Fig. 5 Plot of flow enhancement against pore diameter of each AAM based on (a) mean pore diameter with error span and; (b) the distribution of pore diameter.

A flow enhancement $\varepsilon \sim 1$ for channels with a diameter approaching 100 nm is in agreement with the observation that no slip was seen for pressure driven flow of water in a photoresist coated rectangular channel with a hydraulic diameter of ~84 nm.[43] To the authors' knowledge, no other experimental studies for hydrophilic channels with characteristics sized below 100 nm

have been reported in the literature.

In this study, three factors affecting the extent of flow enhancement have been decoupled, namely the pore diameter, the length of the nanochannels and their wettability. Extrapolation of data in Figure 5a down to the continuum limit yields ε (D_p = 2 nm) ~ 400. The dependence scales with the square of the tube diameter, explaining why little to no enhancement s observed in channels with diameters above 100 nm. This result is entirely consistent with the Hagen-Poiseuille no-slip model in Equation 1 for large channels.

As discussed in the introduction, recent MD simulations have suggested that the flow enhancement factor has a positive correlation with the length of nanotubes.[18] This is indirectly confirmed by comparing results for short[9, 11] and long CNTs,[4, 10] with the latter being 2 to 3 orders of magnitude higher than the former. A similar conclusion has been obtained in the case of alumina nanochannels. In fact, although the variation in thickness between each membrane tends to be small, once the flow enhancement data presented in Figure 5b is normalized to the respective membrane thickness, all data points collapse into a single curve (Figure 6).

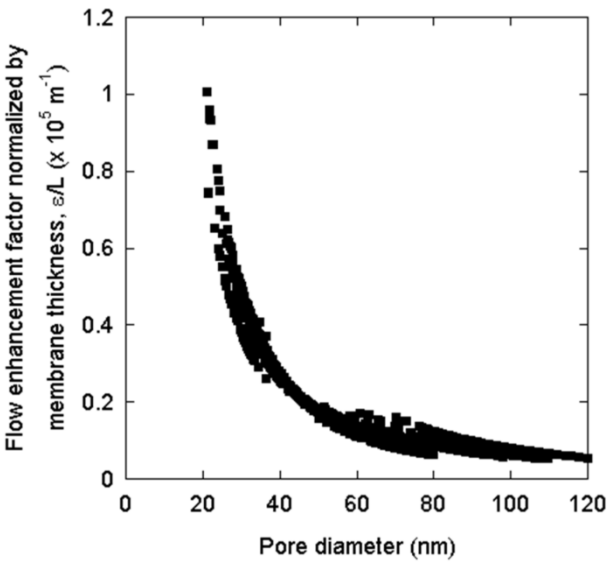

Fig. 6 Plot of flow enhancement factor normalized by membrane thickness against pore diameter of each AAM based on the distribution of pore diameter.

Finally, by comparing the flow enhancement for alumina and carbon nanotube channels of similar diameter and length, it is clearly shown here that the more hydrophilic the material the lower the flow enhancement. As an example, the average flow enhancement for a 40 nm alumina channel normalized by its length is ~0.25×10^5 m^{-1} (Figure 6). This is approximately one order of magnitude smaller than what has been reported for ~44 nm diameter hydrophobic carbon nanopipes (4 - 5×10^5 m^{-1}).[20] A similar difference is obtained when comparing enhancement values for ~2 nm tubes using the extrapolated data from Figure 6 and data for CNTs both from experiments[9] and MD[23].

The above calculations are in agreement with a recent MD paper that relates the occurrence of hydrodynamic slippage, and hence the flow enhancement effect, to the magnitude of solid-liquid molecular interactions and the proximity of preferential adsorption sites on the channel wall that promote the migration of water molecules from one to the next.[28] In fact, the adhesion energy of water on alumina is ~800 mJ m^{-2}, [44] while than on graphite is ~100 mJ m^{-2}, [45] showing significantly lower solid-liquid interaction at the molecular level for water and graphite.[24] In addition, the surface diffusion of water on graphite is also promoted by the smaller distance between neighbouring atoms, 0.14 nm, [46] comparing to that of alumina, 0.18 nm. [47] As shown by a recently proposed mathematical model, low adhesion energy and high surface diffusion induce higher water slippage.[48]

Conclusions

In conclusion, a systematic analysis of pressure-driven water flow through anodized alumina membranes with pores sizes in the 20 nm to 100 nm range (with narrow pore size distribution) has been conducted. Results have shown that flow enhancements, though smaller than for hydrophobic materials such as carbon nanotubes, can be observed for hydrophilic materials as well. The results also confirm that the enhancement increases with decreasing diameter (in particular with the square of the channel diameter) and are a function of the channel length, as predicted by recent molecular dynamics simulations. These results offer a better understanding of fluid transport properties in nanochannels providing important information for various areas of research, including drug delivery, material separations and lab-on-a-chip devices. This work also presents the possibility to develop high permeation hydrophilic membranes, via careful engineering of membrane structures to maximize the flow enhancement effect.

Acknowledgements

The authors acknowledge the University of Bath for supporting this work via the award of an Overseas Research Student Excellence Scholarship to Kah Peng Lee. Additionally we acknowledge the UK EPSRC (grant EP/G045798/1) and the EU (grant PIRG03-GA-2008-230876) for funding support. The contents reflect only the authors' views and not the views of the European Commission.

Notes and references

Department of Chemical Engineering, University of Bath, Claverton Down, Bath, BA1 1UB, United Kingdom. Tel: +44(0)1225383961; E-mail:D.Mattia@bath.ac.uk

1. M. Whitby and N. Quirke, *Nature Nanotech.*, 2007, **2**, 87-94.
2. D. Mattia and Y. Gogotsi, *Microfluid. Nanofluid.*, 2008, **5**, 289-305.
3. T. Myers, *Microfluid. Nanofluid.*, 2010, **10**, 1141-1145.
4. M. Majumder, N. Chopra, R. Andrews and B. J. Hinds, *Nature*, 2005, **438**, 44.
5. M. Majumder, N. Chopra and B. J. Hinds, *ACS Nano*, 2011, **5**, 3867-3877.
6. R. B. Schoch, J. Han and P. Renaud, *Rev. Mod. Phys.*, 2008, **80**, 839.
7. L. Bocquet and E. Charlaix, *Chem. Soc. Rev.*, 2010, **39**, 1073-1095.
8. M. Majumder and B. Corry, *Chemical Communications*, 2011, **47**, 7683-7685.

9. J. K. Holt, H. G. Park, Y. Wang, M. Stadermann, A. B. Artyukhin, C. P. Grigoropoulos, A. Noy and O. Bakajin, *Science*, 2006, **312**, 1034-1037.
10. F. Du, L. Qu, Z. Xia, L. Feng and L. Dai, *Langmuir*, 2011, **27**, 8437-8443.
11. J. A. Thomas and A. J. H. McGaughey, *Nano Lett.*, 2008, **8**, 2788-2793.
12. J. A. Thomas and A. J. H. McGaughey, *Phys. Rev. Lett.*, 2009, **102**, 184502.
13. S. Sinha, M. P. Rossi, D. Mattia, Y. Gogotsi and H. H. Bau, *Phys. Fluids*, 2007, **19**, 013603-013608.
14. A. Striolo, *Nano Lett.*, 2006, **6**, 633 -639.
15. A. Kalra, S. Garde and G. Hummer, *PNAS*, 2003, **100**, 10175-10180.
16. G. Hummer, J. C. Rasaiah and J. P. Noworyta, *Nature*, 2001, **414**, 188-190.
17. B. Corry, *The Journal of Physical Chemistry B*, 2007, **112**, 1427-1434.
18. W. Nicholls, M. Borg, D. Lockerby and J. Reese, *Microfluid. Nanofluid.*, DOI:10.1007/s10404-10011-10869-10403.
19. X. Qin, Q. Yuan, Y. Zhao, S. Xie and Z. Liu, *Nano Lett.*, 2011, **11**, 2173-2177.
20. M. Whitby, L. Cagnon, M. Thanou and N. Quirke, *Nano Lett.*, 2008, **8**, 2632-2637.
21. D. Mattia, M. P. Rossi, B. M. Kim, G. Korneva, H. H. Bau and Y. Gogotsi, *J. Phys. Chem. B*, 2006, **110**, 9850 -9855.
22. D. Mattia, H. H. Bau and Y. Gogotsi, *Langmuir*, 2006, **22**, 1789 - 1794.
23. S. Joseph and N. R. Aluru, *Nano Lett.*, 2008, **8**, 452-458.
24. J. A. Thomas, A. J. H. McGaughey and O. Kuter-Arnebeck, *International Journal of Thermal Sciences*, 2010, **49**, 281-289.
25. T. D. Blake, *Colloids Surf.*, 1990, **47**, 135-145.
26. E. Lauga, M. P. Brenner and H. A. Stone, in *Handbook of Experimental Fluid Dynamics*, eds. J. Foss, C. Tropea and A. Yarin, Springer, New York, 2005, ch. 15th.
27. C. Neto, D. R. Evans, E. Bonaccurso, H.-J. Butt and V. S. J. Craig, *Rep. Prog. Phys.*, 2005, **68**, 2859.
28. T. A. Ho, D. V. Papavassiliou, L. L. Lee and A. Striolo, *Proceedings of the National Academy of Sciences*, 2011, **108**, 16170-16175.
29. L.-J. Cheng and L. Guo, *Microfluid. Nanofluid.*, 2010, **9**, 1033-1039.
30. H. Daiguji, P. Yang and A. Majumdar, *Nano Lett.*, 2003, **4**, 137-142.
31. W. Lu, T. Kim, A. Han, X. Chen and Y. Qiao, *Langmuir*, 2009, **25**, 9463-9466.
32. K. V. Saumitra, X. Dongyan, A. M. Dmitry, P. W. John, H. William and L. Deyu, *Nanotechnology*, 2007, **18**, 275705.
33. N. R. Tas, P. Mela, T. Kramer, J. W. Berenschot and A. van den Berg, *Nano Lett.*, 2003, **3**, 1537-1540.
34. J. H. Park and N. R. Aluru, *Appl. Phys. Lett.*, 2008, **93**, 253104-253103.
35. M.-J. Wei, J. Zhou, X. Lu, Y. Zhu, W. Liu, L. Lu and L. Zhang, *Fluid Phase Equilib.*, 2011, **302**, 316-320.
36. O. Jessensky, F. Muller and U. Gosele, *Appl. Phys. Lett.*, 1998, **72**, 1173-1175.
37. J. P. O'Sullivan and G. C. Wood, *Proc. R. Soc. London, Ser. A*, 1970, **317**, 511-543.
38. H. Masuda and K. Fukuda, *Science*, 1995, **268**, 1466-1468.
39. M. Lillo and D. Losic, *J. Membr. Sci.*, 2009, **327**, 11-17.
40. C. Ran, G. Ding, W. Liu, Y. Deng and W. Hou, *Langmuir*, 2008, **24**, 9952-9955.
41. Z. Li, J. Wang, Y. Zhang, J. Wang, L. Jiang and Y. Song, *Appl. Phys. Lett.*, 2010, **97**, 233107-233103.
42. D. Megias-Alguacil, E. Tervoort, C. Cattin and L. J. Gauckler, *J. Colloid Interface Sci.*, 2011, **353**, 512-518.
43. J. T. Cheng and N. Giordano, *Phys. Rev, E*, 2002, **65**, 031206.
44. P. M. Hobbs and A. J. Kinloch, *J. Adhes.*, 1998, **66**, 203-228.
45. F. M. Fowkes, in *Chemistry and Physics of Interfaces*, American Chemical Society, Washington D.C., 1971, p. 154.
46. C. A. Desch, *The Chemistry of Solids*, Cornell University Press, Ithaca, 1934.
47. S. P. Adiga, P. Zapol and L. A. Curtiss, *PhRvB*, 2006, **74**, 064204.
48. D. Mattia and F. Calabrò, *Microfluid. Nanofluid.*, 2012, 1-6.